Chapter 2

Experimental methods and theoretical Models

2.1 Introduction

During the last decade, the scattering of weakly bound nuclei colliding at energies near and below the Coulomb barrier has been a subject of great interest. The energy dependence of the optical potential (OP) of the elastic scattering of tightly bound nuclei, at near-barrier energies, show a rapid variation of both the real and imaginary parts of the potential. This energy dependence is produced by polarization potentials originated from the coupling between the elastic scattering and different reaction channels, such as inelastic excitations, transfer of nucleons, breakup etc. Around the Coulomb barrier perusal of elastic scattering angular distribution is important to obtain the energy dependence real and imaginary optical potential parameters of the nuclear reactions. From the methodical investigation of elastic scattering angular distribution measurements for tightly bound nuclei, that is known as threshold anomaly (TA) [1, 2, 36, 37] and for weakly bound projectile known as breakup threshold anomaly [3, 21, 38].

In the present thesis, TA and BTA have been experimentally studied followed by its theoretical interpretation using optical model parameters. The experiments have been carried out using the facilities of the 14UD Bhabha Atomic Research Centre-Tata Institute of Fundamental Research (BARC-TIFR) pelletron accelerator facility

at Mumbai. A brief description about the accelerator facilities is presented in this chapter. The development in heavy ion accelerator has been matched by continuous improvement in the detection techniques which has eventually made it possible to disentangle the information contained in the reaction products, to a high degree of accuracy. In the present thesis several detectors have been used and their characteristics are discussed briefly. The particle identification techniques, pulse shape discrimination, time of flight method have also been discussed.

The Pelletron Accelerator facility in Mumbai, has been serving as a major facility for heavy ion accelerator based research in India since its commissioning in December 1988. In this accelerator, the maximum terminal voltage is 14 MV. The high electric voltage at the terminal is achieved by means of the chain of steel pellets separated by insulators and hence the name **Pelletron Accelerator**. The details are given in various literatures [39, 40, 38, 41].

2.2 Accelerator facility

2.2.1 The pelletron accelerator

Fig.2.1 shows the schematic diagram of the 14UD BARC-TIFR pelletron accelerator facility, in Mumbai [42]. The ion source named 'SNICS' (Source of Negative Ions by Cesium Sputtering), situated at the top of the accelerator tower generates negative ions which are initially accelerated to low energies (150–250 keV) in short horizontal section [43]. These low energy negative ions are then mass analyzed using a 90° magnet (injector magnet) before entry into the vertical accelerator column. These injected ions gets accelerated towards the positively charged high voltage terminal situated in the middle. Due to this acceleration, negative ions gains an energy of V_T MeV, where V_T is the terminal voltage in MV (million volts). This high electric potential at the terminal is achieved by means of the chain of steel pellets separated by insulators and hence the name Pelletron accelerator. This method leads to more uniform charging

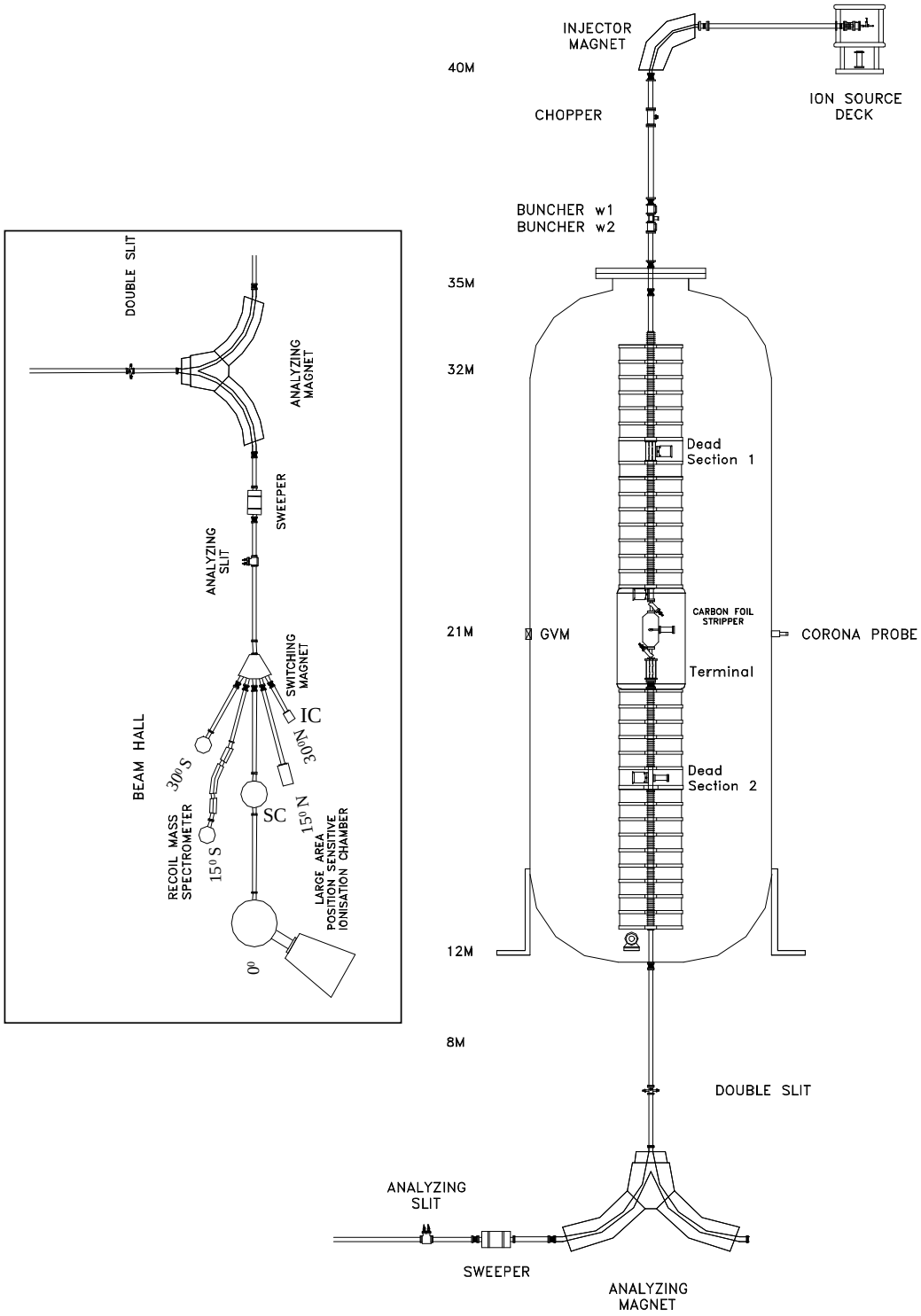

Figure 2.1: Schematic drawing of the Mumbai Pelletron accelerator facility. The left panel of the figure shows the 5 beam lines.

compared to moving charging belt and hence less ripple on the HV terminal. Inside the terminal, the ions pass through a thin carbon foil ($\sim$ 5 μg/cm^2) or a small volume of a gas, where they loose several electrons resulting in distribution of positively charged ions. This distribution depends on the type and velocity of the ions. These positively charged ions at the terminal are repelled by the positive voltage at the terminal and are therefore accelerated to the ground potential. This results in a energy gain of qV_T MeV for a ion with charge q. Thus, the total energy gain of the ions becomes;

$$E = (q + 1) \times V_T \quad \text{MeV}. \tag{2.1}$$

At the end of the accelerating tube, an analyzing magnet is placed which serves the purpose of charge and energy selection of the ion. The energy of the analyzed ions of mass number A and charge state q in this accelerator is given by the relation [44]

$$B = 720.76\frac{\sqrt{AE}}{q}. \tag{2.2}$$

where B is the magnetic field in Gauss and E is the energy in MeV. This analyzed beam of ions is then transported to the experimental setup with the help of switching magnet.

There are five beam lines in the accelerator facility as listed below:-

1. 30° North, used for irradiation of nuclear targets and other samples for radiochemical, material and biological studies. Also used for AMS measurements.

2. 15° North, used for gamma-ray, neutron and charge particle spectra measurements.

3. 0°, consist of a general purpose scattering chamber (used to measure cross-sections and angular distributions for various nuclear reactions). This is further extended to house one small scattering chamber with a large area position sensitive deep ionization chamber (used for fission study).

4. 15° South, dedicated for recoil mass separator.

5. 30° South, used for gamma-ray, charge particle and atomic physics measurements.

Measurements presented in this thesis were carried out in 0° beam line using the general purpose scattering chamber.

2.2.2 FOTIA accelerator

The principal mechanism of this accelerator [45, 46] is similar to the pelletron accelerator. In FOTIA (Folded Tandem Ion Accelerator), the negative ions are produced (from the cathode sample) by cesium sputtering, extracted and pre-accelerated up to 150 keV. The singly charged negative ions selected through the 70° magnet are injected into the low energy accelerating tube through the 20° electrostatic deflector (see Fig.2.2). The electrostatic quadrupole triplet and the einzel lens focus the beam to match its parameters to the acceptance of the low energy accelerating tube. The negative ions are accelerated to the positively charged high voltage (up to 6 MV) terminal and lose some of the electrons while passing through the foil stripper (that is kept inside the terminal dome) to become positive ions. The positive ions of particular charge state are bent through the 180° folding magnet, and then again accelerated through the high energy accelerating tube to the ground potential. The diverging beam at the exit of the high energy accelerating tube is focussed by the magnetic quadrupole triplet, and then analyzed by the 90° bending magnet.

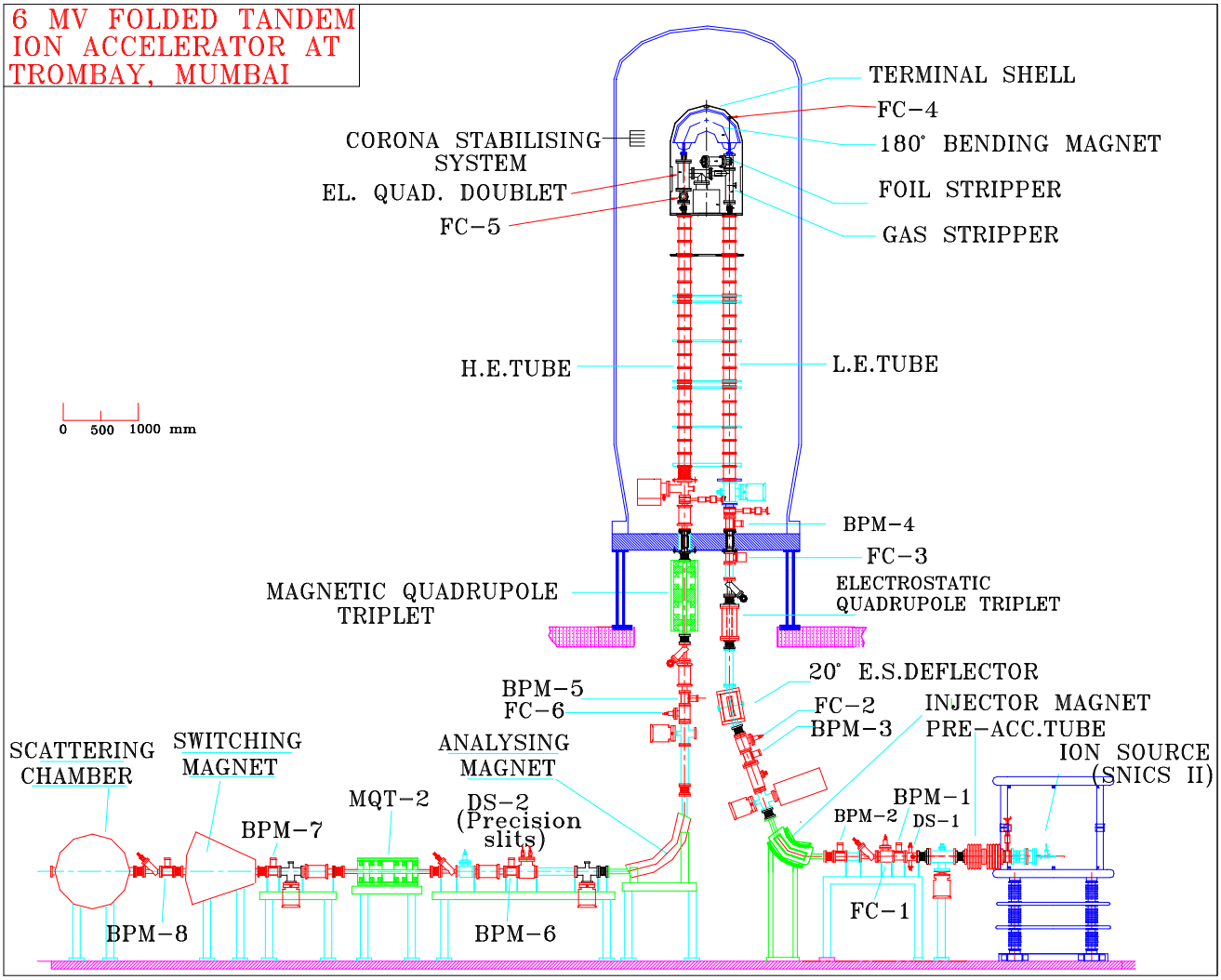

Figure 2.2: Schematic diagram of the 6 MV Folded Tandem Ion Accelerator.

The analyzed beam is guided to the scattering chamber through the second magnetic quadrupole triplet and the switching magnet.

2.3 Types of detectors

2.3.1 Gas detectors

The gas detectors are the simplest devices used for the detection of radiation. The striking features of the gas detectors in comparison to other type of detectors are the versatility of construction in various configuration, variation in thickness by selecting appropriate gas pressure, and immunity to the radiation damage. The simplest form of a gas detector is essentially a parallel plate capacitor in which the region between the plates is filled with a gas suitable for ionization when a radiation passes through it. As ionizing radiation passes through the gas volume, it dissipates some or all of its energy in collisions with the gas molecules, and thus creates electron and positive ion pairs. In the absence of the electric field between the plates, the motion of electrons and positive ions would be random, and they would even mutually recombine to form neutral molecules. However, when a voltage is applied between the plates, the electrons are accelerated and acquire a net drift velocity in the direction of the anode plate. Likewise, the positive ions acquire a net velocity in the direction of the cathode plate. The space charge resulting from the reaction of the electron-ion pairs and their subsequent motion within the electric field,causes an induced electric current at the electrode plates. This induced current continues to flow until all of the charge has been collected. Measurement of the induced current or voltage pulse provides the detector signal.

Behavior of the gas detector varies as a function of applied electric field. With all other parameters being fixed (detector geometry, gas type, pressure, etc.) the gas detectors exhibit different characteristics in the different domains of the applied field as shown in the Fig.2.3 from [47]. Fig.2.3 shows the pulse amplitude as a function of the applied field, displaying the different regions of the gas detector operation such as,

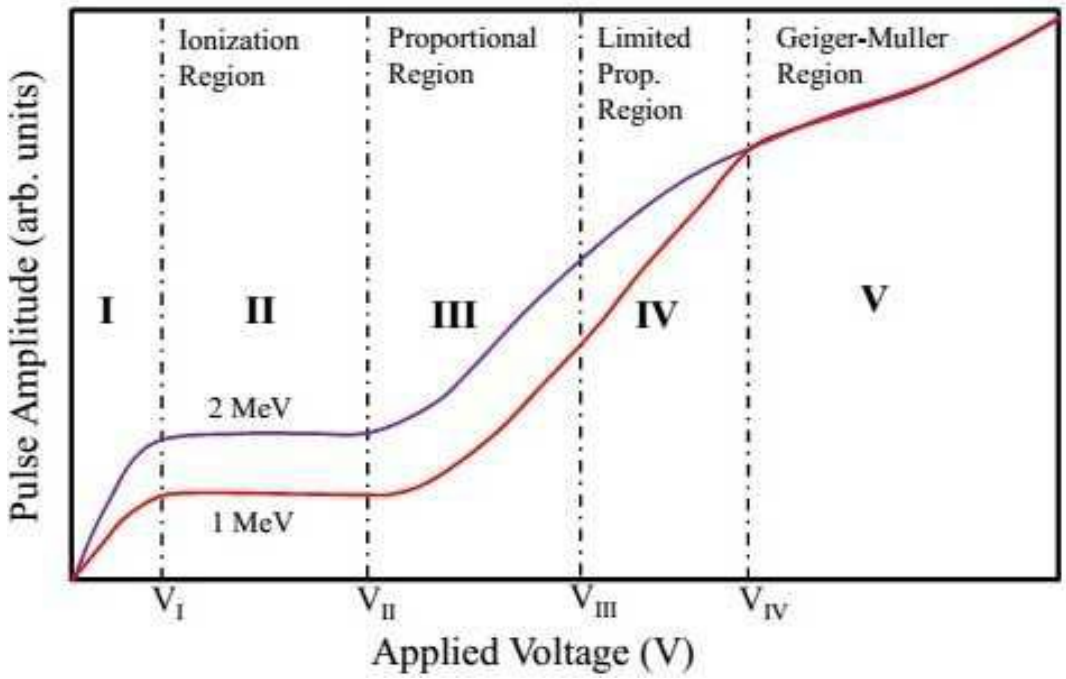

Figure 2.3: The different regions of operation of a pulse mode gas detector. The pulse amplitude is plotted for two different energies of the radiation.

Ionization, Proportional, Limited Proportional, and the Geiger-Mueller (GM) region.

2.3.2 Scintillator detectors

The scintillation detector is one of the most useful particle detection devices in nuclear physics today. It is comprised of two main components: first, a scintillator which absorbs incident radiation and converts the energy deposited by ionization into a fast pulse of light, and second, a photomultiplier. This second component converts the light pulse into a pulse of electrons and also amplifies the electron pulse to be recorded or processed. Many different types of scintillators exist for example, an organic liquid solution, a plastic, or a crystal (organic or inorganic). The light output of a scintillator is proportional to the deposited energy so the amplitude of the electrical signal will be proportional to this energy [47, 48].

When manufacturing proton recoil scintillators, the choice of some sort of organic scintillator is obvious[48]. The first scintillators used for neutron spectroscopy were anthracen and stilbene crystals. Anthracen has the highest scintillation efficiency of all organic scintillators and one usually states the scintillation efficiency in percentages of that of anthracen. Stilbene was used when pulse shape discrimination techniques were desired. One great disadvantage of anthracen and stilbene is the anisotropy in scintillation efficiency; the light output is dependent on the charged particles direction relative to the crystal axis. This will, of course, spoil the energy resolution. Also anthracen and stilbene are difficult and thus expensive to manufacture in large sizes. Nowadays, proton recoil scintillators in a liquid or a solid form are both cheap and easy to manufacture in different shapes and sizes. The liquid scintillator basically consists of an organic scintillator dissolved in an appropiate solvent. Often, activators and wavelength shifters are added.

2.3.3 Organic scintillator detectors

Liquid organic scintillators mainly consist of aromatic hydrocarbons, with small admixtures of other molecules. In aromatic hydrocarbons two types of chemical bonds are important, σ bond and π bond. The σ bonds are the normal regular tetrahedron bonds of carbon and they do not contribute to the luminesence of the liquid, whereas the π bonds cause double and triple bonds and are responsible for the luminesence. In aromatic hydrocarbons there are many "p" orbitals which make up a de-localized π system that can be modeled as free electron orbiting the nucleus. The scintillation light comes from transitions of molecular valence electrons between different energy levels. The energy levels are separated into spin singlet levels (S_0, S_1 , S_2 ...) and spin triplet levels (T_1, T_2 ...). Every molecular energy level has associated vibrational energy levels, (S_{00}, S_{01} ...; S_{10}, S_{11} ...) and (T_{10}, T_{11} ...) (see Fig.2.4).

The energy difference between molecular energy levels is of the order of $\sim$ 3 eV, while the difference between vibrational energy levels is $\sim$ 0.1 eV. When ionizing radiation passes through the scintillator, the molecules may absorb a fraction of the energy with their p orbital electrons via transitions from the ground state to higher energy levels. Electrons excited to higher energy levels rapidly (few $\sim$ ps) fall back to the S_1 level via radiation-less de-excitation.

Scintillation light is emitted due to the de-excitation of electrons from S_1 level to one of the vibrational states of the ground state S_0 (fluorescence). This type of transition occurs with decay times $\sim$ ns, corresponding to the fast component of the scintillation light pulse. The other possibility is an inter-system crossing decay. In this case, the electron in S_1 level crosses to T_1 level and from there this molecule interacts with an other molecule with an electron in T_1 state. The result of such an interaction leaves one molecule in the S_1 state and the other in the S_0 state. The life time of T_1 ($\sim$ ms) is characteristically much longer than that of S_{10}. So the radiation emitted

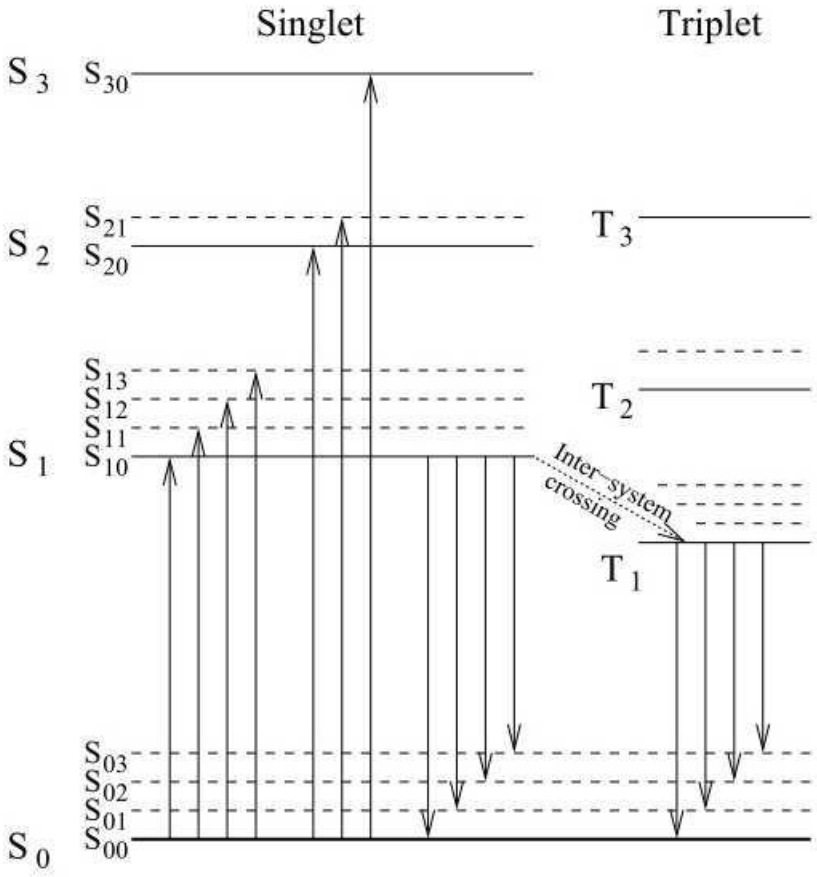

Figure 2.4: Typical energy levels diagram of an organic scintillator.

(phosphorescence) in the de-excitation does not contribute to the pulse produced by the prompt fluorescence. However, instead of a transition to S_0, some of the molecules can be excited back to S_{10} and then decay to S_0, which is called delayed fluorescence. Decay time in this case is $\sim$ 100 - 500 ns. The scintillation light is the superposition of two or more exponential decay components with different decay time constants. Delayed fluorescence constitutes the slow component of the scintillation light and is mainly responsible for the neutron gamma discrimination property of liquid scintillator.

2.3.4 Semiconductor detectors for charge particle detection

For the spectroscopy of charged particles, the semiconductor detectors have been extensively used due to the following advantages-

1. Semiconductors have a very small band gap energy of ($\sim$1 eV). Thus electron-hole pair generation due to the impinging radiation is easier as compared to the electron-ion pair generated in gas detectors, used for charged particle measurements.

2. The time required for the electrons and holes to be collected at the respective terminals is considerably less, due to their high drift velocities, as compared to the time required for the electrons and ions to be collected. This enables the use of semiconductor detectors to give better timing characteristics and their use in experiments requiring fast timing.

3. Their larger detector material density allow for generation of more electron-hole pairs as opposed to ionization chambers and have greater stopping power.

4. Semiconductor detectors are compact in size.

The basic working principle of a semiconductor detector is as follows:-
These detectors are basically *p-n* junction diodes, which are operated in the reverse

biased condition. This is because, for a reverse biased *p*-*n* junction, the depletion region is heavily exhausted of majority charge carriers. Thus, any radiation impinging on the detector will create ionization, generating the electron-hole pairs and thus giving an electrical signal. The energy accrued by the incident particle in the detector is directly proportional to the amplitude of the signal, and the time required for collection of such events gives the time information [49].

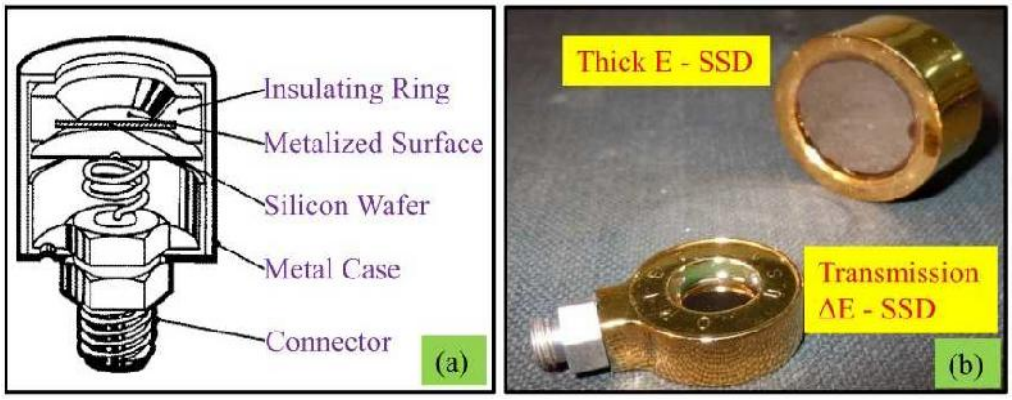

Figure 2.5: Schematic (a) and real (b) views of typical silicon surface barrier detector.

For charged particle detection silicon (Si) is the most widely used material due to its slightly higher band gap energy of $\sim$ 1.1 eV as compared to germanium (Ge) having a band gap energy of $\sim$ 0.7 eV. Thus, it can be used even at room temperature. The silicon surface barrier (SSB) detectors are the widely used detectors for charged particle measurements. Fig.2.5 show the schematic diagram of silicon surface barrier detector.

In these detectors, a *p*-*n* junction is formed between a semiconductor and a metal, usually *n*-type silicon with gold or *p*-type silicon with aluminum [48]. Due to the different Fermi levels of these materials, a contact emf arises when the two are put together. This leads to lowering of the band levels in the semiconductor region and thus extension of the depletion region entirely into the semiconductor region. Such junctions are also called as Schottky barrier and possess many of the characteristics of the *p*-*n* junction [48]. These detectors are fabricated at room temperature by first etching the silicon surface and then depositing a thin layer ($\sim 40 g/cm^2$) of gold by

evaporation. The surface is also allowed to oxidize before the deposition. The junction is then mounted in an insulating ring with metalized surfaces for electrical contacts. SSBs can be fabricated with varying thickness and depletion region. For fully depleted detector, in which the depletion region extends entirely into the thickness of the silicon wafer, serves as a transmission detector for measuring the energy deposition of a passing particle. Increasing the bias of such detectors helps in faster charge collection and thus a fast signal rise time. Commercially available SSB detectors have thickness between a few tens of μm to few mm.

In the present thesis work, we have used silicon surface barrier detectors for charge particle detection.

2.4 Interaction of charge particles with matter

The charged particles interact mainly by the Coulomb forces between their positive and the negative charge of the orbital electrons within the detector material [47]. Upon entering the detector, the charged particle immediately interacts with many electrons of the detector material. Depending on the energy of the incident particle, the atoms of the detector material may either be excited to higher states or completely removed due to ionization. Repeated interactions within the detector thus leads to loss of energy of the charged particle and they finally are stopped. The electrons emerging from these interactions represent this energy lost by the charged particles. The energy loss *i.e.*, the mean stopping power S, of any detector material, for a charged particle is given by $S = -\frac{dE}{dx}$. Thus energy loss increases with decrease in energy of the charged particle within the detector material and is given by the Bethe-Bloch Formula[47, 48],

$$-\frac{dE}{dX} = \frac{4\pi e^4 z^2}{m_0 v^2} NB \tag{2.3}$$

where,

$$B \equiv Z\left[ln\frac{2m_0v^2}{I} - ln\left(1-\frac{v^2}{c^2}\right) - \frac{v^2}{c^2} - s - D\right] \tag{2.4}$$

where v and ze are the velocity and charge of the primary particle, N and Z are the no. density and atomic no. of the atoms of the detector material, m_o is the electron rest mass and e is the electronic charge. I represents the mean excitation potential for the detector material. s is the correction factor taking into account the non availability of electrons to be ionized by equal probability from different shells. D is the density correction factor.

2.5 Particle identification

Identification of different reaction products is one of the primary requirement in the study of nuclear reaction mechanism. Energy loss measurement is one of the efficient techniques used for this purpose. This technique is based on the fact that for different particles of same energy, the specific energy loss (-dE/dX) on passing through the different material is different. In this technique, the particles are first allowed to traverse through thin transmission type detector, where the partial energy (ΔE) is lost and the remaining energy of the incident particle is deposited in the E detector, hence technique is referred as $\Delta E - E$ technique. The thickness of the ΔE detector is chosen very small compared to the incident particle range. The schematic diagram of this telescope arrangement of ΔE and E detectors is shown in Fig.2.6.

The (-dE/dX) of the charge particle on passing through the medium is described by the well known Bethe-Bloch formula given by Eq.2.3. For non relativistic particles, $v^2 = 2E/M$ and since the logarithmic term varies only slowly with energy [50], a further simplification leads to;

$$\frac{\mathrm{dE}}{\mathrm{dx}} \propto \frac{\mathrm{AZ}^2}{\mathrm{E}}. \tag{2.5}$$

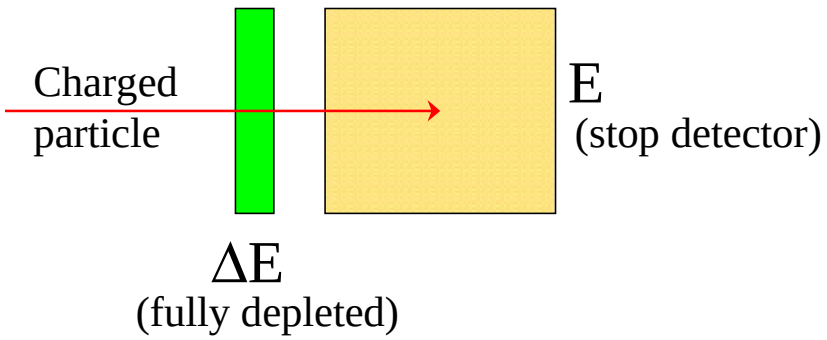

Figure 2.6: Schematic diagram showing ΔE-E telescope setup. ΔE is generally thin solid state detector or gas detector so as to pass the incident particle and E detector is thick solid state detector chosen to stop the remaining energy of incident particle.

This energy loss principle is used in the $\Delta E - E$ telescopic configuration to identify the mass and charge of the reaction products. For different elements, the energy loss will be different at a given energy and will vary according to Eq.2.5. Thus, the spectrum from a $\Delta E - E$ detector shows bands separating each element according to its charge and mass. The ΔE is a thin detector, in which the particle losses some fraction of its total energy and finally stops in the E detector, which is a thick detector, in which it deposits its remaining energy. Thus, addition of energies from both these detectors gives the total incident energy of the detected particle.

The approximation made in Eq.2.5 is not applicable always. However, an empirical power law,

$$\frac{1}{\mathrm{Z}^2}\frac{\mathrm{dE}}{\mathrm{dx}} \propto \left(\frac{\mathrm{E}}{\mathrm{A}}\right)^{-0.73} \tag{2.6}$$

was found to be a good approximation to Bethe-Bloch formula for most light ions over a wide range of values of E/A. The Eq.2.6 can be integrated over the particle range to get a range-energy relation,

$$\mathrm{R} = \mathrm{aE^b}. \tag{2.7}$$

where, 'R' is the range and the constant 'a' is approximately proportional to $1/\mathrm{AZ}^2$ (if the ion is fully stripped). The index 'b' is always found to be less than 1.73 and varies slowly with the energy E.

In order to determine the atomic no. Z and mass no. A using the $\Delta E - E$ telescope configuration, identifier algorithms are required which combine the detector signals to give a single unique output where the size represents the type of ion detected. Eq.2.5 gives;

$$(\mathrm{E} + \Delta\mathrm{E})\frac{\Delta E}{\Delta X} \propto \mathrm{MZ}^2 \tag{2.8}$$

This implies that for all signals from the detector, a unique pattern proportional to MZ^2 will be obtained in the spectrum. However, the slow variation of the logarithmic term is not negligible and thus a modified form of Eq.2.8 is required to generate the

spectrum,

$$(\mathrm{E} + E_0 + k\Delta\mathrm{E})\frac{\Delta E}{\Delta X} \propto \mathrm{MZ}^2 \tag{2.9}$$

where E_0 and k are adjustable parameters chosen to make the output signal as energy independent as possible over the range of particles and energies investigated in the experiment.

Using Eq.2.7 the range of the particles can be found as,

$$(\mathrm{E} + \Delta\mathrm{E})^b - E^b = \frac{T}{a} \tag{2.10}$$

where T is the ΔE detector thickness and a $\propto (1/\mathrm{MZ}^2)$ for a fully stripped ion. This range-energy relationship is valid over the range and energies of ions for which the power law holds *i.e.*, b=constant and the identifier signal (T/a) remains constant over a broad energy range.

2.6 Experimental setup

All the experiment reported in this thesis were performed using the 14UD Pelletron facility of Bhabha Atomic Research Centre and Tata Institute of fundamental research (Mumbai). The experiments were performed on four projectiles ^{6,7} Li and ^{10,11}B on very heavy mass target ^{232}Th. Measurements of elastic, quasi elastic and transfer angular distribution were done in the energy range of around the Coulomb barrier. The details of the measurements of elastic, quasi elastic and transfer angular distribution are given in chapters 3 and 4 respectively.

The Schematic block diagram of the experimental setup is shown in Fig.2.7. This is used for the measurements of elastic scattering, quasi elastic and transfer angular distributions. For these measurement four silicon surface barrier detectors were used at different angles.

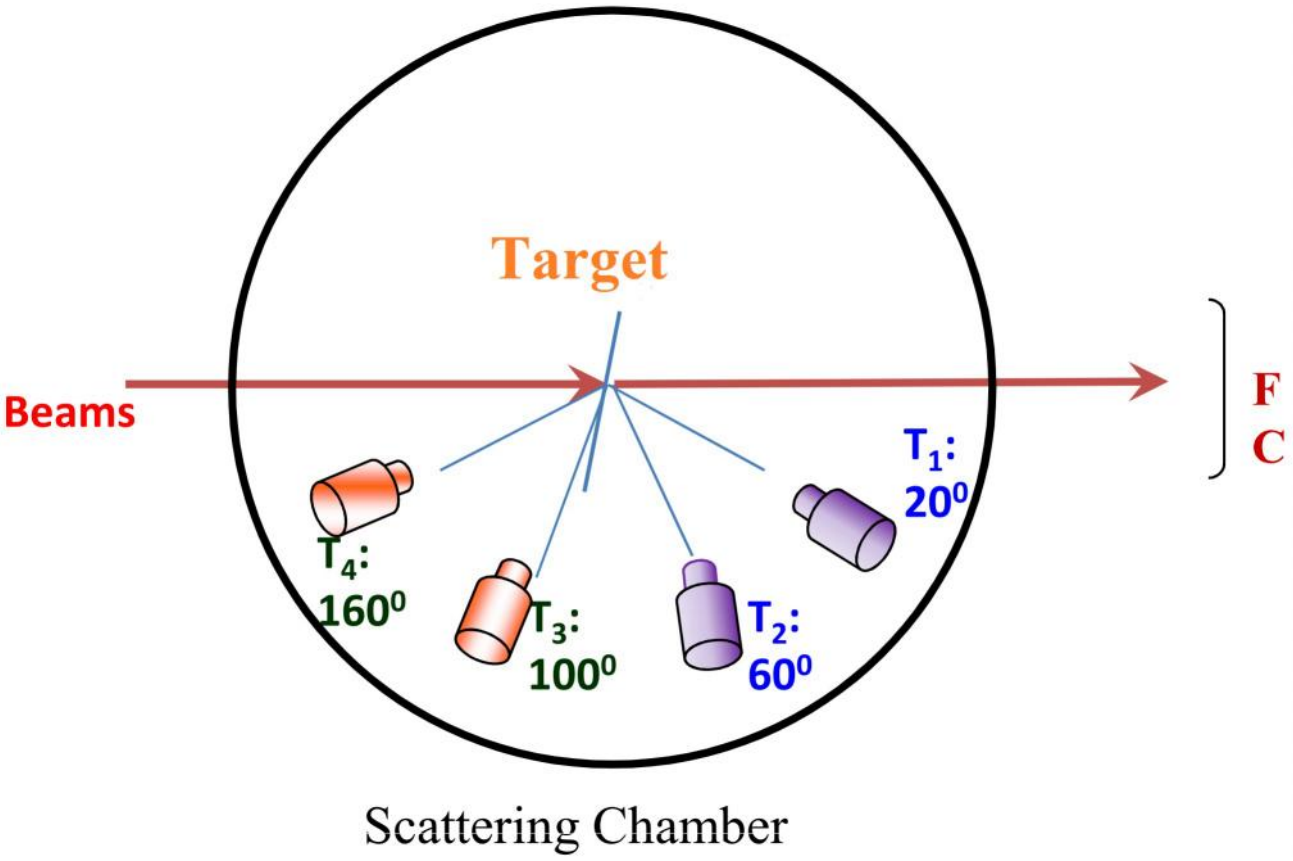

Figure 2.7: Schematic block diagram of the experimental setup for the elastic scattering, quasi elastic and transfer angular distribution measurements.

2.6.1 Experimental arrangement

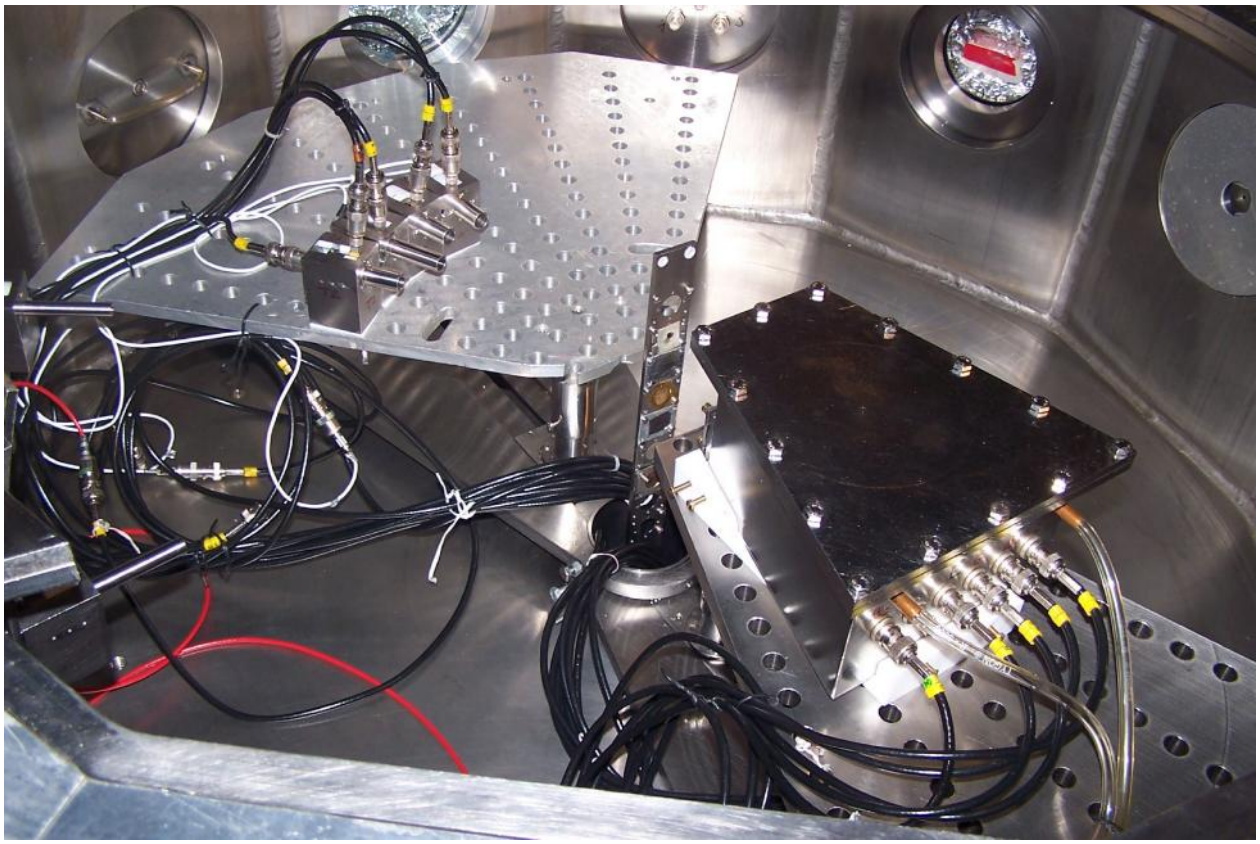

Figure 2.8: Four silicon surface barrier detectors telescopes placed on the one movable arm of the scattering chamber and target ladder and gas detector also shown in the figure.

The Figs.2.8 and 2.9 show the pictures of scattering chamber and setup of detectors for the measurement of elastic scattering and transfer angular distribution. In the experiment we have used four silicon surface barrier detectors and two monitor with different thickness. Detectors mounted on scattering chamber in the movable arm and monitor detector fixed at forward angle. The target ladder mounted inside the 1 m (approx) diameter scattering chamber. Charge particles detected by silicon surface barrier detector in different angles at various energies. In this thesis we have used four beams ^{6,7}Li and ^{10,11}B in two different experiments. In the first experiment we have taken ^{6,7}Li beams in the wide range of energies. The beam energy for ^{7}Li + ^{232}Th reaction is 24, 26, 30, 32, 35, 40, and 44 MeV and for ^{6}Li + ^{232}Th system is 26, 30, 32, 35, 40, and 44 MeV. The beams ^{6,7}Li were bombarded on self supporting target ^{232}Th. The thickness of the target was 1.6 mg/cm^2, which has been mounted on center in a scattering chamber. Throughout the experiment the current of the beam was nearly 20 to 40 nA. For the detection of elastic scattering of ^{6,7}Li ions, four silicon surface barrier detectors used. These detectors mounted on scattering chamber in the movable arm. The Fig.2.8 and 2.9 show the scattering chamber and setup of detectors for the measurement of elastic scattering. In the experiment we have used four silicon surface barrier detectors with different thickness, which is given for each telescope (1) For telescope (T_1) ΔE = 25 μm and E = 300 μm, (2) for telescope (T_2) with ΔE = 15 μm and E = 1500 μm, (3) for telescope (T_3) with ΔE = 15 μm and E = 1000 μm, and (4) for telescope (T_4) with ΔE = 15 μm and E = 1000 μm were used in the experiment. The separation of detector telescope was 10°. We have used two monitor detectors at $\pm$15° with respect to the beam direction. In the second experiment we have measured the quasi-elastic scattering and transfer angular distribution by using ^{10,11}B beams at different bombarding energies E_{lab} = 52, 53, 54, 55, 56, 57, 59, 61 and 65 MeV for ^{11}B + ^{232}Th system and 49, 51, 52, 53, 54, 55, 56, 57, 59, 61 and 65 MeV for ^{10}B + ^{232}Th system. For this experiment we have used self-supporting target^{232}Th with 1.3 mg/cm^2 thickness. In this measurement we have

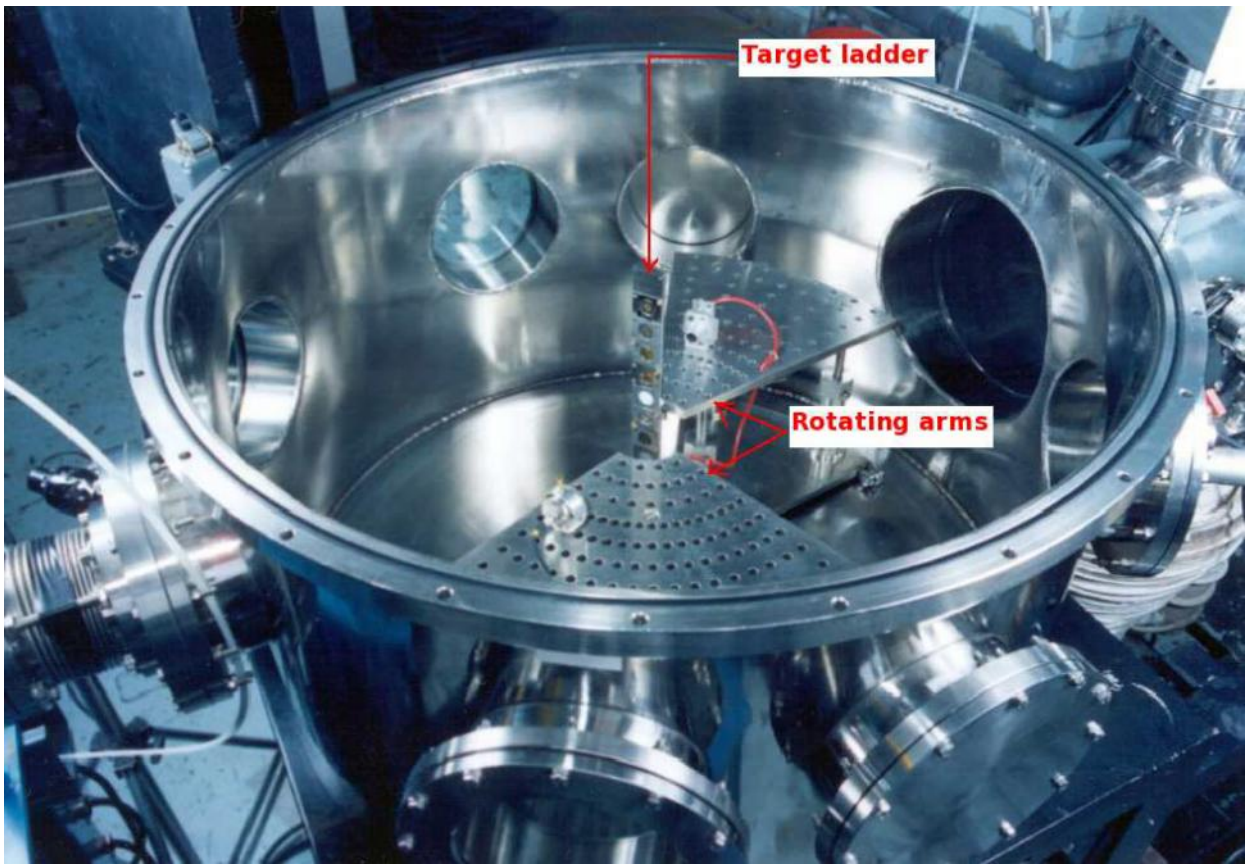

Figure 2.9: Scattering chamber of elastic scattering angular distribution experiment.

used four SSB (silicon surface barrier) detector telescopes with different thickness. For telescope (T_1) the thickness was $\Delta E = 25$ μm and E = 0.3 mm, for telescope (T_2) the thickness was $\Delta E = 40$ μm and E = 0.3 mm, for telescope (T_3) thickness was $\Delta E = 25$ μm and E = 0.3 mm) and for telescope(T_4) thickness was $\Delta E = 25$ μm and E = 0.3 mm. The angular separation of telescopes were 10° in the scattering chamber. The front collimator of telescope was 6 mm and angular uncertainty was ± 0.81.We have used two monitor detectors in this experiment with thickness 300 μm were and 1 mm collimator. The monitor detector was mounted at ± 18° in the beam direction on the scattering chamber. The purpose of monitor detector was to have complete normalization and monitor the beam. The angles put in order from 35° to 170° in the steps of 5°.

Experimental data analysis, results and discussion will be presented in chapter 3 and 4 respectively for both experiments.

2.6.2 Electronic setup description

Fig.2.10 shows the schematic block diagram of the electronic set up, using the E-ΔE detector telescope. Identical to Fig.2.10, all other three E-ΔE detectors were arranged in the similar way inside the scattering chamber. The incident beam coming with high energy interacts with the target and measured by the detector. The detectors have the specific volume, and therefore produce electrical signals in the output circuit. Primarily signals are smaller than required, therefore amplification of signals is needed. The slow output which coming from the preamplifier are used to scaling the energy which deposited in the detector. Therefore, from each detector telescope, via coaxal cables, the signal which is emitted by preamplifier now reaches to the amplifier. The amplifier is used to give shape using inbuilt RC and CR circuits and amplifies the signal. For the timing information output of the ΔE detectors is connected to the preamplifier and the fast ouput which coming from preamplifier is connected to the Timing Filter Amplifier. The Timing Filter Amplifier filters the signal from the preamplifier and also preserve

the fast output pulse shape thereby not affecting the high frequency components. The outputs that are coming from the Timing Filter Amplifier of all the ΔE detectors are connected to the Constant Fraction Discriminator with a delay cable to get delayed output. The work of delayed output is that to stop signal and the corresponding start signal was taken from the main trigger for Time to Digital Converter. All the output from Constant Fraction Discriminator, through the logic OR gate, are connected to the Gate and Delay Generator, where the main common gate is built and given as master strobe to the Analog to Digital Converter. Analog to Digital Converter converts all the analog signal to the equivalent digital form, thus its a fundamental link between analog and digital electronics [48]. Then, with the help of BUS, the digital signals from ADC are sent to the the data acquisition system called LAMPS [51]. LAMPS (Linux Advanced Multi parameter system) is widely used for data acquisition and analysis. It can also be used for off line data analysis.
The description of electronic setup is given follows

2.6.2.1 Preamplifier

A preamplifier (preamp) is an electronic amplifier that converts a weak electrical signals from a detector and shape the output pulses. Preamp reduce the effect of noise. It is mounted as close as possible to the detector so minimize the cable length. The important work of preamp is that present the correct impedance to the detector and the electronics [48, 47].

2.6.2.2 Amplifier

The amplifier serves two main purposes- 1) Amplification of the signal from the preamplifier and 2) Shaping the amplified signal for further processing. The amplifiers basically contain a series of RC and CR circuits which provide the shaping of the preamplifier pulse. In addition, they also help in pole zero cancellation in which an undershoot

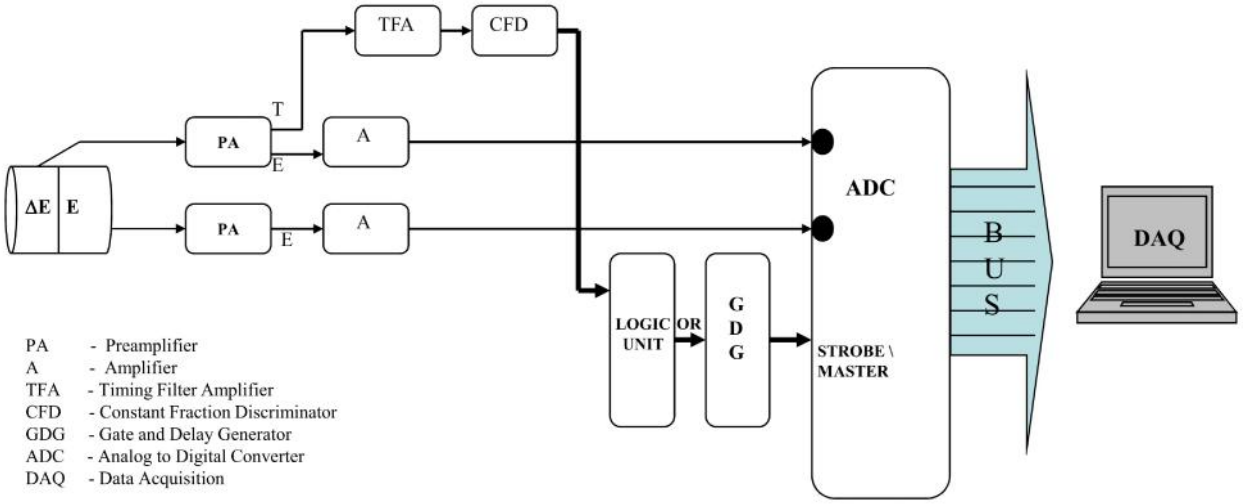

Figure 2.10: Schematic block diagram of the complete electronic set up corresponding to a typical experimental set up as shown in Fig (2.7).

arising due to the RC shaping is removed. The amplifiers used for processing the energy signal are linear amplifiers i.e., the amplitudes of the output signal from these amplifiers is linearly proportional to the energy of the impinging radiation [47, 48].

2.6.2.3 Timing filter amplifier

When timing information from a signal is required, a fast linear pulse of short duration from the detector output is chosen [47, 48] . This type of pulse is commonly supplied to a leading edge of a time pick-off unit to provide a prompt timing signal. In order for the time pick-off unit to trigger on receiving such a signal, the input from the detector needs to have a sufficient strength in terms of amplitude. The amplifiers used for shaping cannot be used in this case since they are designed to eliminate the high frequency components in the signal for optimum amplitude resolution. Thus, to preserve the fast linear pulse shape, an amplifier with a linear response to as high frequency components as possible is required. The TFA helps in processing these fast linear pulse shapes and in addiction, also provides a small degree of filtering of the signal from the preamplifier. The TFA provides some amplitude gain and adjustable differentiation and integration constant that are typically much shorter (200 ns or less) than those present in linear amplifiers. The output pulses from the TFA have faster rise times, smaller widths and provide good coupling to the time pick-off units [47, 48].

2.6.2.4 Constant fraction discriminator (CFD)

CFDs are the time pick-off units which provide a logic output, whose leading edge indicates the time of occurrence of the input linear pulse. These devices help in elimination of time jitter and amplitude walk. The time jitter occurs when pulses have the same amplitude but have a random noise contribution, due to which the signal pulse size and shape fluctuates. Amplitude walk arises when two pulses have identical time of origin but give rise to output logic pulses that differ substantially in their timing due to difference in pulse height which trigger a trigger unit set at some fixed level. Both

these effects are eliminated by the CFD in which the output pulse from the TFA is attenuated by some fraction of the original pulse height, inverted, delayed and added back to the original TFA pulse. This leads to a fixed time of crossing for all the pulses, even if they have slightly different pulse heights [47, 48].

2.6.2.5 Analog-to-digital converters(ADC)

ADCs provide processing of the analog signals (signals continuous in time) coming from the amplifiers to digital output.The logic gate has been used to give a logic OR output of all the timing signals from all the ΔE detectors and given as a master to the ADC. In this way, the random events are eliminated and the time for which the ADC is busy processing the incoming signals, is optimized to process signals only coming at correlated time between the telescopes. The digital signals from the ADCs have been further processed by the softwares LAMPS (Linux Advances Multi parameter System) [51] in other to generate the graphical spectrum from the digital pulses of the ADCs [47, 48].

2.7 Theoretical models used in the thesis

2.7.1 Nuclear models

The nucleus represents a finite self-bound thermionic many-body quantum mechanical system. The observable properties of such a body and its microscopic structure are a complex function of many degree of freedom. Therefore, models are inevitable for making predictions and inter predictions of experimental data. A number of nuclear models have been proposed with different sets of assumptions and each of them could explain some experimental observations. Presently, no single model can explain all the observations. In this chapter, one of the theoretical models relevant to the present work has been discussed.

2.7.2 Optical model

Optical model was proposed nearly six decades ago to describe the nuclear scattering and reaction phenomena. The optical model has a significant impact on many branches of nuclear reaction physics. This is called '*Optical model*' by analogy with the treatment of the scattering of light by a refracting and absorbing medium using a complex refractive index. The central assumption of this model is that the complicated interaction between an incident particle and a target nucleus can be represented by a complex mean-field potential, which divides the reaction flux into a part covering shape elastic scattering and a part describing all competing non-elastic channels. Solving the Schrödinger equation with this complex potential yields a prediction for the basic observables, namely, the elastic scattering angular distribution and total reaction cross-sections. An important feature of good optical model potential is that it can be used to reliably predict these observables for energies and nuclides for which no experimental measurement data exist. Moreover, the quality of several derived quantities that are provided by the optical model has an important impact on the evaluation of the various non-elastic channels. Well-known examples are the related transmission coefficients that enter the statistical model of compound nucleus evaporation, and the distorted wave functions that are used for the description of direct inelastic scattering to discrete states as well as in evaluations of multistep direct transitions to the continuum. The reaction cross-sections that are calculated with the optical model are important for the evaporation part of intranuclear cascade models, statistical models and also for semi-classical pre-equilibrium models. Therefore, it is crucial that the optical model potentials that enter such nuclear model calculations be adequately determined. This model has been very successful in interpreting a large body of projectile-target interaction data in terms of a complex nuclear potential (Woods Saxon Potential) [10, 11, 40, 52].

2.7.2.1 Woods Saxon Potential

The Woods-Saxon potential is a mean field potential for the nucleons (protons and neutrons) inside the atomic nucleus, which is used to describe approximately the forces applied on each nucleon, in the nuclear shell model for the structure of the nucleus.

The form of the potential, as a function of the distance r from the center of nucleus, is:

$$U(r) = -(V_c + iW_c)f(r, r_o, a) \tag{2.11}$$

$$U(r) = \frac{-(V_c + iW_c)}{1 + exp\frac{(r-R)}{a}} \tag{2.12}$$

V_0, W_0, R and a are the optical model parameters. The real part V_0 always represents the strength of potential which causes the elastic scattering and the imaginary part W_0 gives the strength of absorptive potential through all non-elastic channels which accounts for the loss of incident flux. This absorption may be of different kinds depending upon the energy and the structure of the interacting particles. In some cases, the absorption is of surface type while in other cases of volume type or a combination of both. The other two parameters R and a are called as half value radius and the diffuseness respectively.
This Fig.2.11 shows the Woods Saxon graph of real part of the optical potential parameters.

The wave functions associated with the scattered particles are calculated from the optical potential by solving the Schrdinger equation.

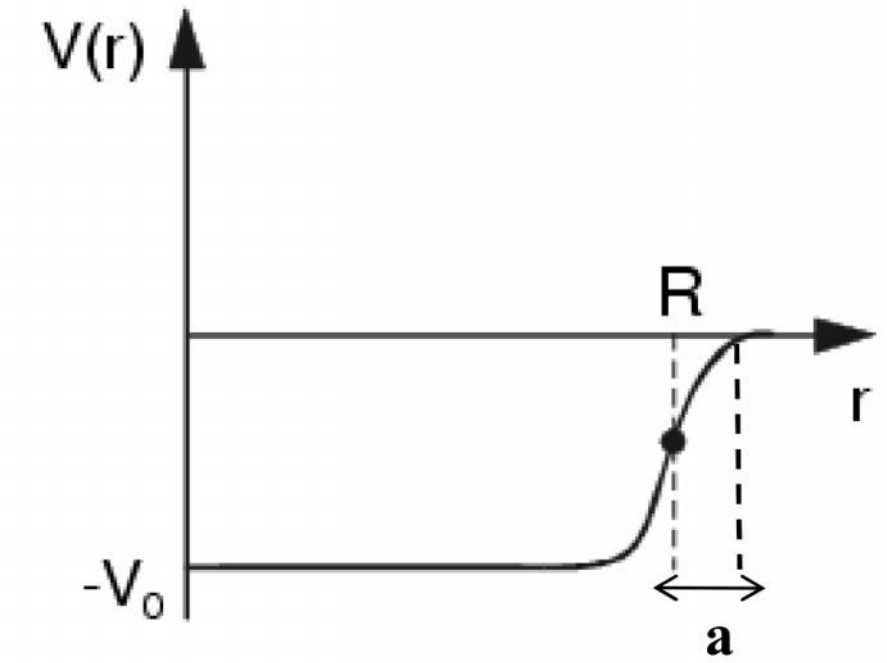

Figure 2.11: Woods and Saxon potential graph shown in eq.(2.12)

$$\bigtriangledown^2\psi + \frac{2m}{\hbar^2}[E - V_{opt}(r)]\psi = 0 \tag{2.13}$$

Considering the total wave function ψ as a combination of an incident plane wave and a spherical scattered wave. This may be done by expanding ψ in partial waves. These equations may be integrated numerically for each values of l contributing to the interaction and the resulting (complex) radial wave functions are matched to the known asymptotic form beyond the nuclear field to obtain the scattering matrix element η_l.

The observable quantity can be described as,

$$\frac{d\sigma(\theta)}{d\Omega} = |f(\theta)^2| \tag{2.14}$$

where,

$$f(\theta) = f_c(\theta) + \sum_{l=0}^{\infty}(2l+1)(\eta_l - 1) \tag{2.15}$$

in which $f_c(\theta)$ is the Coulomb scattering amplitude. The expression for elastic scattering (σ_{EL}), reaction cross-section (σ_R) and total reaction cross-section (σ_{tot}) can be written as follows [7, 10, 11]:

$$\sigma_{El} = \pi\lambda\!\!\!^{-2}\sum_{l=0}^{\infty}(2l+1) \mid 1 - \eta_l \mid^2 \tag{2.16}$$

$$\sigma_R = \pi\lambda\!\!\!^{-2}\sum_{l=0}^{\infty}(2l+1)(1- \mid \eta_l \mid^2) \tag{2.17}$$

$$\sigma_{CN} = \pi\lambda\!\!\!^{-2}\sum_{l=0}^{\infty}(2l+1)(1-\eta_l)^2 \tag{2.18}$$

$$\sigma_T = \sigma_{El} + \sigma_R \tag{2.19}$$

$$\eta_l = exp(2i\delta_l) \tag{2.20}$$

Here $\lambda\!\!\!^{-}$ is called the reduced de-Broglie wavelength δ_l is a complex number representing the phase shift between the outgoing and the ingoing waves.

2.7.2.2 Sao Paulo Potential

The optical potential plays a central role in the description of heavy-ion collisions, since it is widely used in studies of the elastic scattering process as well as in more complicated reactions through the distorted-wave Born approximation or coupled-channel formalisms. This complex and energy-dependent potential is composed of the bare and polarization potentials, the latter containing the contribution arising from nonelastic couplings. In principle, the nuclear potential between two heavy ions can be associated with the fundamental nucleon-nucleon interaction folded into a product of the nucleon densities of the nuclei [53] The Sao Paulo potential (SPP), which is a kind of folding model potential that takes into account the Pauli principle due to exchange of nucleons between the projectile and target, is another theoretical model for the heavy-ion nuclear interaction. In principle, the bare (or nuclear) potential between two heavy ions can be associated with the fundamental nucleon nucleon interaction folded into a product of the nucleon densities of the nuclei [9]. The Sao Paulo potential has been successful in describing the elastic scattering and peripheral reaction channels for a large number of heavy-ion systems in a very wide energy region, from sub-Coulomb to 200 MeV/nucleon. It has also described the total reaction and fusion cross sections for hundreds of systems. Within this model, the nuclear interaction is connected with the folding potential through [54, 55, 56, 57, 58, 59, 27].

V(r) is the DF (double folding) potential carried out by introducing the effective nucleon-nucleon (NN) interaction over the ground state DD (density distribution) of the two colliding nuclei. It is evaluated from the expression

$$V_{fold}(R) = \int \rho_1(\vec{r_1})\rho_2(\vec{r_2})v(\vec{NN})d\vec{r_1}d\bar{r_2} \tag{2.21}$$

where v($\vec{r}$)=V_o δ ($\vec{R}$-$\vec{r_1}$+$\vec{r_2}$)

where ρ_1 ($\vec{r_1}$),ρ_2 ($\vec{r_2}$)are the nuclear matter density of the two colliding nuclei, and

and v($\vec{NN}$) is the effective nucleon-nucleon interaction. v($\vec{NN}$)is taken to be a standard Reid- M3Y interaction [53] in the form,

$$V_{NN}(r) = 7999.0\frac{e^{-4.0r}}{4.0r} - 2134.0\frac{e^{-2.5r}}{2.5r} + J_{oo}(E)\delta(r) \tag{2.22}$$

The first and second terms represent the direct part and the third term represents the exchange part of the interaction potential. It plays an important role in reproducing the experimental results for elastic and inelastic scattering [53, 60, 61].

$$J_{oo}(E) = -276(1 - 0.005E/A) \tag{2.23}$$

where E is the energy in the center of mass system and A is the mass number of the projectile.

The total potential must comprise both the real part and the imaginary part, the latter is being responsible for the absorption of the incident particle in the channels.

$$U(r) = N_r V_{(r)} + N_i W_{(i)} \tag{2.24}$$

Since the interaction is real, the folding calculation gives the real and imaginary parts of the potential. The volume real and imaginary parts have the folded form with normalization factors $N_{(r)}$ and $N_{(i)}$.

2.8 Method to obtain the elastic scattering cross-sections

According to the non-relativistic energy rule, the Schrodinger's equation is applied

$$\Delta^2\Psi + \frac{2\mu}{\hbar^2}[E - V(r)]\Psi = 0 \tag{2.25}$$

The equation of radial wave, can be written as,

$$\frac{d^2u}{dr^2} + [k^2 - \frac{l(l+1)}{r^2} - \frac{2\mu V(r)}{\hbar^2}]u(r) = 0 \tag{2.26}$$

where u = rψ , k^2=2$\mu/\hbar^2$ and V=V$_{Coul}$-V$_{Nucl}$

To drive this equation the interaction region is divided into two parts the internal region means where nuclear force acting and the external region means where nuclear force free. The two are contacted at a convenient distance called the matching radius. Beyond this radius, the nuclear potential is considered to be negligible. Usually, this matching is done at a value roughly given as R(half value radius) + 10a (the diffuseness) R and a are parameters of the nuclear potential. In the internal region, numerical integration of the Schrodinger's equation is carried out using standard integration techniques like the Runge-Kutta method, Fox-Goodwin, etc. The first and the second values (i.e., u_1 and u_2) are $u_n = 0$ and $u_{n+1} = r^{j+1}$ at r = h where h is the integration step size and h=matching radius/no. of steps used in the integration. Typically h=0.1 fm. Knowing u_1 and u_2, the higher u_l are calculated for each higher particle wave l. The numerical integration proceeds up to the matching radius. In the external region beyond the matching radius, the solutions of the schrodinger equation are the Coulomb functions for charged particles and Bessel/Neumann functions for neutrons. The internal and external wave functions and their derivatives are matched at the matching radius to yield the scattering matrix S. S is complex and given by $S_l = e^{2i\delta_l}$ where $\pm$l is the phase shift which is complex. The transmission coefficient T is calculated from the S matrix using T_l=1-S_l^2.Using these S matrix elements, the differential elastic scattering cross-section and the reaction cross-section are calculated using:

$$A(\theta) = f_c(\theta) + \frac{i}{2k}\sum_{l=0}^{\infty} e^{2i\delta_l}[(1+S_l^+) + l(1-S_l^-)]P_l cos\theta \tag{2.27}$$

$$B(\theta) = \frac{i}{2k}\sum_{l=0}^{\infty} e^{2i\delta_l}[S_l^+ \pm S_l^-]P_l cos\theta \tag{2.28}$$

$$\frac{d\sigma_{el}}{d\Omega} = |A(\theta)|^2 + |B(\theta)|^2 \tag{2.29}$$

where f_θ and δ_l are the coulomb scattering amplitude and phase shift respectively. The reaction cross-section is calculated by

$$\sigma = \frac{\pi}{k^2} \sum_{l=0} [(l+1)T_l^+ + lT_l^-] \tag{2.30}$$

where ± stands for j=l ±1/2. For a spinless particle, B θ=0 and from equations, it can be seen that the differential elastic scattering cross-section is related to S or the phase shift, which in turn is decided by the potential energy and particle type. Thus, the phase shift provides a connecting link between experiment and theory.

2.9 Dispersion relation

Dispersion Relation analysis is important for correlated behaviors of real V(E) and imaginary W(E) optical potential parameters at near the Coulomb barrier. The relation is

$$\Delta V(E) = \frac{P}{\pi} \int_{-\infty}^{+\infty} \frac{W(E')}{E' - E} dE' \tag{2.31}$$

Also,

$$V(E) = V_o + \Delta V(E) \tag{2.32}$$

where, P is the principal value of the integral, V(E) is dynamical real potential, ΔV is dynamical polarization potential. V_o is independent of energy and W(E) is energy dependent imaginary potential.

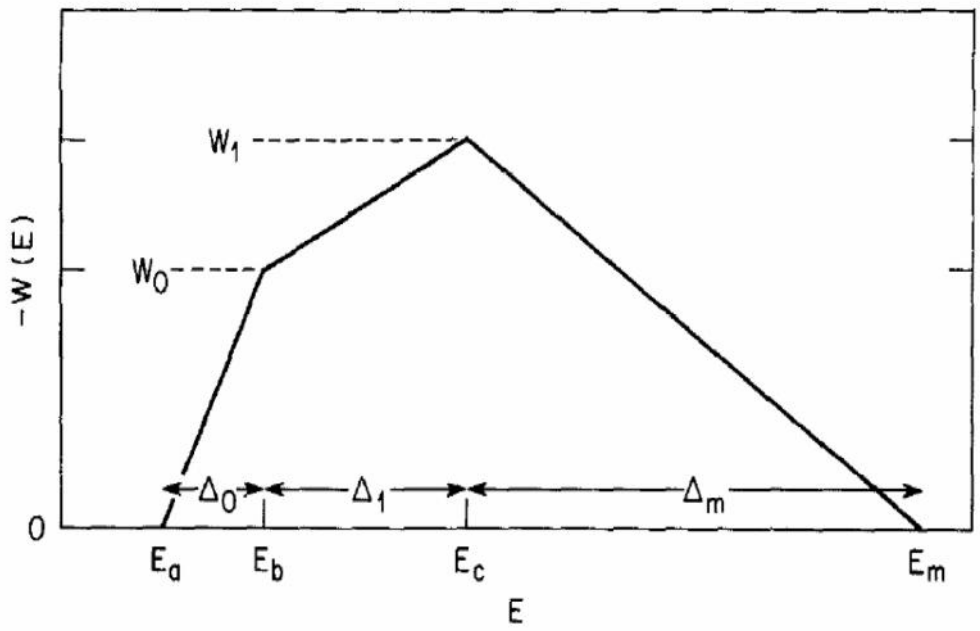

Figure 2.12: The linear schematic model for W (E), consisting of three straight line segments (19).

From the analysis of elastic scattering angular distribution got optical potential parameters V_r and V_i real and imaginary respectively. These optical potential parameters show rapid variation around the Coulomb barrier. If the real optical potential parameters increases and corresponding imaginary optical potential parameters are decreases as the incident energy decrease towards the Coulomb barrier. This phenomena known as "Threshold anomaly" (TA) as shown in Figs (1.3) and (1.4) of chapter 1, this process has been distinguishable in condition of pairing of elastic channel to the other direct reaction channels that procreate an attractive polarization potentials at around the Coulomb barrier [21, 3, 38]. Now, in the study of loosely bound projectile contrary indication have been present at around the Coulomb barrier where, the real optical potential parameters decreases and corresponding imaginary optical potential parameters are increases as the incident energy decrease towards the Coulomb barrier. This behavior understand in the condition of pairing of breakup reaction channels to the elastic scattering, This process is called "breakup threshold anomaly" (BTA) as shown in Figs (1.5) and (1.6) of chapter 1 [21, 3, 38].

The dispersion relation method has been used as a function of energy at radius of sensitivity to the optical potential parameters, demarcated at every energy.

For practical calculation of the dispersion relation, the linear segment model [19] is used where W(E) is composed of three or more linear segments as shown in Fig.2.12

E_b in the figure represents the reference energy. For any energy E_s

$$\Delta VE_s(E) = \Delta V(E) + \Delta V(E_s) \tag{2.33}$$

Each line segment associated with an increment W_{ij}=W(E_i)- W(E_j) yields a contribution to Δ V(E),

$$\Delta V_{ij}(E) = (\frac{W_ij}{\pi})[\epsilon_i \ln|\epsilon_i| - \epsilon_j \ln|\epsilon_j|] \tag{2.34}$$

where $\epsilon_i = \frac{E-E_i}{\Delta_{ij}}$, $\epsilon_j = \frac{E-E_j}{\Delta_{ij}}$and Δ_{ij} = E_j-E_i. Thus,

$$\pi\Delta V(E) = W_0[\epsilon_0 \ln|\epsilon_a| - \epsilon_b \ln|\epsilon_b|] + (W_1 - W_0)[\epsilon_b^{'} \ln\left|\epsilon_b^{'}\right| - \epsilon_c^{'} \ln\left|\epsilon_c^{'}\right|] \tag{2.35}$$

$$W_1[\epsilon_c^{"} \ln|\epsilon_c^{"}| - \epsilon_m^{"} \ln|\epsilon_m^{"}|] + W_1[\eta \ln \eta - (\eta+1)\ln(\eta+1)] \quad (2.36)$$

where W_o,W_1 $\geq$0 and $\epsilon_i = \frac{E-E_i}{\Delta_0}$, $\epsilon_i^{'} = \frac{E-E_i}{\Delta_1}$, $\epsilon_i^{"} = \frac{E-E_i}{\Delta_m}$ and $\eta = \frac{\Delta_1}{\Delta_m}$.

By putting in the line segments for the imaginary part of potential, the real part of potential is calculated. This processes has used in the dispersion relation calculations carried out for the threshold anomaly/breakup threshold anomaly [1, 40, 19].

2.10 Study of channel-coupling and polarization potential by elastic scattering

When the couple reaction channel projection (with all the significant reactions coupled) match with the experimental elastic scattering cross sections at different energies around the Coulomb barrier, it is contained that, the channel-coupling impact generate the same character which gives rise to the threshold anomaly in the usual optical model treatment. It would be admirable if this say energy dependence of the optical potential near the threshold (to inelastic and transfer reactions) could be mention from the couple reaction channel computations in a way which is more transpicuous and is readily perceived and matched. It is always probabilistic to inclusive the effect of channel couplings in the elastic optical potential parameters by means of a polarization potential. The sum of this and the bare potential contemplate for the elastic channel in the couple reaction channel computations should be equal to the optical potential extractive from the fit to the experimental elastic scattering angular distribution data [1, 39].

,